Wrinkled Flower-Like rGO intercalated with $Ni(OH)_2$ and MnO_2 as High-Performing Supercapacitor Electrode

Yeasin Arafat Tarek, Ragib Shakil, Akter Hossain Reaz, Chanchal Kumar Roy, Hasi Rani Barai, and Shakhawat H. Firoz*

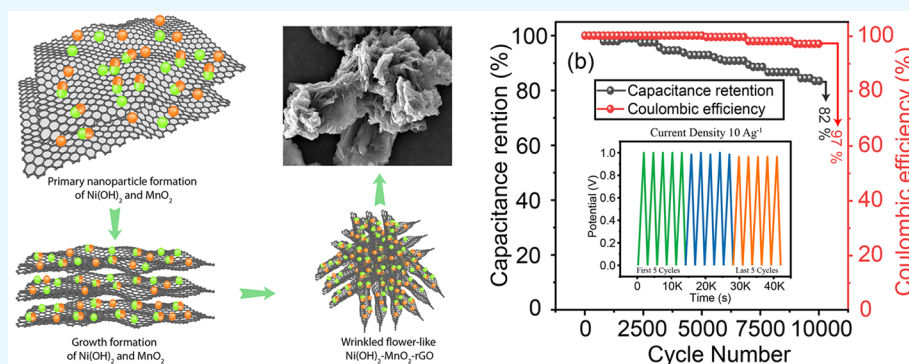Cite This: *ACS Omega* 2022, 7, 20145−20154

Read Online

ACCESS | 📊 Metrics & More | 📰 Article Recommendations | SI Supporting Information

ABSTRACT: This study reports a simple one-step hydrothermal method for the preparation of a $Ni(OH)_2$ and MnO_2 intercalated rGO nanostructure as a potential supercapacitor electrode material. Having highly amorphous rGO layers with turbostratic and integrated wrinkled flower-like morphology, the as-prepared electrode material showed a high specific capacitance of 420 F g^{-1} and an energy density of 14.58 Wh kg^{-1} with 0.5 M Na_2SO_4 as the electrolyte in a symmetric two-electrode. With the successful intercalation of the γ-MnO_2 and α-$Ni(OH)_2$ in between the surface of the as-prepared rGO layers, the interlayer distance of the rGO nanosheets expanded to 0.87 nm. The synergistic effect of γ-MnO_2, α-$Ni(OH)_2$, and rGO exhibited the satisfying high cyclic stability with a capacitance retention of 82% even after 10 000 cycles. Thus, the as-prepared $Ni(OH)_2$ and MnO_2 intercalated rGO ternary hybrid is expected to contribute to the fabrication of a real-time high-performing supercapacitor device.

■ INTRODUCTION

Supercapacitors (SCs) are the futuristic technology in the heavy-duty energy storage sector because of their efficient power and energy density, longer cyclic stability, and minimal risk of explosion, properties which are unlike batteries.[1,2] Nevertheless, the electrochemical nature and stable performance of a high-performance SC are mostly determined by the three-dimensional spatial arrangement of the electrode materials used during the fabrication of SC.[3] Smooth insertion/desertion of electrolyte ions into the electrode surface during the electrochemical charge storing process is crucial for storing massive energy. That is only possible with an extremely tailored morphological design of the electrode materials.[4,5] However, research shows that the nanostructured ternary hybrids of carbon material (activated carbon, rGO, CNT, MWCNT, SWNT, etc.) with multiple transitional-metal oxides/hydroxides (TMO/H) viz., Co_2O_3, MnO_2, NiO, Mn_2O_3, $Mn(OH)_2$, and $Ni(OH)_2$, are much more special than a single component carbonaceous or a TMO/H electrode. The hierarchal morphological attributes of the ternary hybrids showed the ability to generate more accessible pores and interlayer spacing because of the coexistence of amorphous and crystalline planes. Usually, those features also provide smooth mobilization of electrolyte ions into the hybrid electrodes during both charging and discharging. Thus, the fabrication of ternary hybrid electrode is now considered an excellent pathway for drawing higher electrochemical performance and outstanding cyclic stability.[6−8]

Now, the selection of the TMO/H and carbonaceous material for synthesizing any ternary hybrid always plays a crucial role to attain high-performance in SC devices. Among various pseudocapacitive TMO electrode materials, the MnO_2 nanoparticle is an excellent choice because of its low cost, high abundance, and easy preparation.[8] Besides, it shows multiple oxidation states with different tunnel-like morphological attributes which facilitates greater electrolyte accessibility.

One of the interesting properties regarding manganese oxide is that it can form a heterostructure in which the interfacial properties can be tuned in a controlled manner.[9] For instance, it has been seen that the intercalation of another nanoparticle can significantly contribute to further enhancement of MnO_2 based supercapacitors.[10] Especially, the intercalation of Ni-$(OH)_2$ as a guest nanoparticle in MnO_2 matrix has been seen to induce a conducting network throughout the binary composite which can increase the rate capability and capacitive performance.[11,12] For instance, Huang et al. demonstrated that the intercalation of $Ni(OH)_2$ into the MnO_2 matrix has significantly improved the accessibility of electrolytes and transportation of electrons in the binary composite electrode compared with the pure MnO_2 electrode material.[13] Several studies have proved that the redox reactions during the charging/discharging process are the key to showing high capacitance for the binary composites of the $Ni(OH)_2$-MnO_2.[14,15] Unfortunately, the binary composites of Ni-$(OH)_2$-MnO_2 always suffer from cyclability issues because of those unavoidable abrupt parasitic redox reactions with electrolytes.[16] Now, this problem can easily be resolved by intercalating the binary TMO/H composites with another conductive and tailored carbonaceous network. This approach always showed an increase in the overall charge transfer rate and high performance while retaining the morphology of the ternary hybrid by suppressing the destructive effect of fast-reversible redox reactions induced from the TMO/H.[17−19]

However, among other carbonaceous materials, a reduced graphene oxide (rGO) nanosheet is always one step ahead for outstanding features such as facile synthesis approach, high surface area, greater conductivity, better mechanical strength, and high thermal and chemical stability.[20,21] As rGO nanosheet stores the electrochemical charge by forming an electric double layer (EDL), its amorphous and layered structure remains the same even after several thousand cycles while maintaining high specific capacitance with high power and energy density.[22,23] Then, one may ask why pure rGO is not a preference in the way of fabricating SC? It is worth mentioning that the synthesis of pristine rGO by the conventional chemical reduction method is quite tedious and needs extreme sophistication because of its intensive interlayer stacking tendency.[24,25] This property leads to the agglomeration of rGO and significantly reduces the surface area, conductivity, surface activity, and poor electrochemical performance. So, the intercalation of TMO/H such as $Ni(OH)_2$ and MnO_2 in between the rGO brings about some distinctive morphology features like more accessible channels, pores, and defects.[26,27] In addition, this intercalation enhances the total surface area of rGO by expanding its interlayer distance and generating turbostratic structures throughout the rGO layers.[28,29] These synergistic effects of $Ni(OH)_2$, and MnO_2 in between rGO layers facilitate more interlayer space and hence smoother movement of electrical charge in the electrode−electrolyte interface. Thus, this intercalation renders the scope to improve SC performance significantly. Additionally, it resolves the cyclability problem simultaneously by protecting the $Ni(OH)_2$ and MnO_2 from excessive self-aggregation and redox reactions.[30,31]

Therefore, ongoing efforts are focused on developing an effective method for the scalable production of ternary $Ni(OH)_2$-MnO_2-rGO (NMr) hybrid. Unfortunately, most of the synthesis process reported earlier for intercalating Ni-$(OH)_2$ and MnO_2 in between rGO is tedious and followed by multiple critical steps. In this work, a one-step hydrothermal method was introduced to synthesize the ternary hybrid nanostructure of NMr. Surprisingly, the synthesized ternary hybrid exhibited a highly amorphous and wrinkled flower-like nanostructure with exceptional SC performance, making it suitable for the production of real-time SC devices.

■ EXPERIMENTAL SECTION

Materials and Chemicals. Potassium permanganate ($KMnO_4$), nickel nitrate hexahydrate ($Ni(NO_3)_2·6H_2O$), glycerol, sulfuric acid (H_2SO_4), polyvinylidene fluoride (PVDF), hydrogen peroxide (H_2O_2), hydrochloric acid (HCl), graphite powder, ethanol (C_2H_5OH), N-methyl-2-pyrrolidone (NMP), and sodium sulfate (Na_2SO_4) were purchased from Merck, Germany and used without further purification.

Synthesis of GO, rGO, and NMr Ternary Hybrid. The GO was prepared according to the modified Hummer's method.[32] The ternary hybrid of NMr was synthesized by adopting a straightforward one-step gel-forming hydrothermal method. Briefly, a 25 mL of $Ni(NO_3)_2·6H_2O$ (0.5 mmol) solution was mixed with glycerol (5 mL). Then, the mixture was slowly added to a 50 mL of $KMnO_4$ (0.3 mmol) solution containing a homogeneous aqueous suspension of GO (0.2 g) under vigorous magnetic stirring, followed by the addition of extra H_2O (3.0 mL) and glycerol (10 mL). Following that, the precursor was moved into a 100 mL Teflon autoclave. The autoclave was then sealed and maintained at 180 °C for 24 h to enable the formation of NMr hybrid. After that, the gel-like product was washed with ethanol and DI water and dried in a hot-air oven (80 °C) to obtain the desired ternary NMr hybrid. For comparison, pure rGO from GO was also synthesized by the same hydrothermal process at 180 °C for 24 h without using nickel nitrate and potassium permanganate.

Characterization of Materials. NMr sample was studied by XRD (Rigaku Ultima IV, Japan) using Cu Kα radiation and running at a constant current of 40 mA and a constant voltage of 40 kV to explore phase transformations and crystallographic structures. An FESEM (TESCAN LYRA 3, Czech Republic) and HRTEM (JEM-2011, JEOL, Japan) were used to study the morphologies of NMr hybrid. To perform energy-dispersive X-ray spectroscopy (EDX), an Xmass detector with the FESEM was employed. At ambient temperature, a Raman spectrometer (iHR320, HORIBA, JAPAN) with a CCD detector and a green-light laser (300 mW) with an excitation wavelength of λ_o = 532 nm was used to analyze the graphitic/defective architectures of the carbon samples. The elemental analysis on the NMr sample was conducted produced by using the Thermo Scientific ESCALAB 250Xi XPS Microprobe, which was fitted with an Al Kα microfocusing X-ray monochromator. The electrochemical characterizations of NMr was done by using CHI 660E.

Fabrication of Electrodes and Electrochemical Measurement. The electrochemical behavior of the as-prepared NMr ternary hybrid was investigated in a standard symmetric two-electrode system in an aqueous 0.5 M Na_2SO_4 electrolyte at room temperature. A disk-shaped graphite plate as a current collector and Whatman filter paper (pore size, 11 μm) as a separator was used. The symmetrical two-electrode cell setup and electrode fabrication process are described in our earlier works.[33−36] The specific capacitance (C_{sp}), energy density (E), and power density (P) values of the symmetrical two-electrode
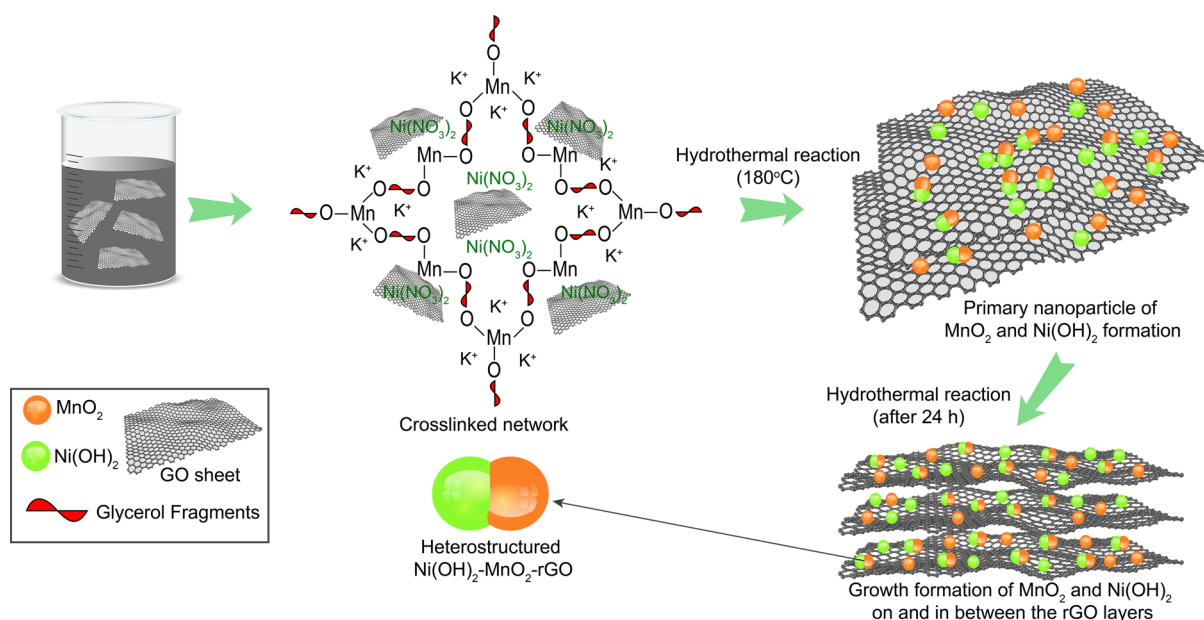
Figure 1. Growth formation mechanism of Ni(OH)$_2$, MnO$_2$ in between the hybrid rGO layers.

system as employed were from the GCD results using the following eqs 1−3:

$$C_{sp} \ (\text{F g}^{-1}) = \frac{2I\Delta t}{m\Delta V} \tag{1}$$

$$E \ (\text{Wh kg}^{-1}) = \frac{C_{sp}\Delta V^2}{28.8} \tag{2}$$

$$P \ (\text{W kg}^{-1}) = \frac{E \times 3600}{\Delta t} \tag{3}$$

where I = applied current on the active material, Δt = discharge time, m = active mass on each electrode, ΔV = working potential window. The capacitance retention and the Coulombic efficiency were calculated by using eqs 4 and 5, respectively.

$$\text{capacitance retention} = \frac{n^{\text{th}} \text{ cycle capacitance}}{1^{\text{st}} \text{ cycle capacitance}} \times 100 \tag{4}$$

$$\text{Coulombic efficiency}, \ \eta = \frac{t_{\text{discharge}}}{t_{\text{charge}}} \times 100 \tag{5}$$

■ RESULTS AND DISCUSSION

Formation of NMr Ternary Hybrid. The possible formation mechanism of NMr ternary hybrid is depicted in Figure 1. In the first phase, the GO suspension containing KMnO$_4$ reacted with glycerol (having nickel nitrate solution) to form a cross-linked gel network. The cross-linked network was generated from the instantaneous reaction of KMnO$_4$ and glycerol. Ullah et al. stated the coexistence of manganese oxides sites (Mn^{2+}, Mn^{3+}) with some partially oxidized glycerol fragments in the cross-linked network.[37] As the formation of this cross-linked network occurred within the GO environment, it is expected that the Mn^{2+}, Mn^{3+} were distributed homogeneously in between the GO surface because of the electrostatic interaction between the GO layers. Until now,

Ni(NO$_3$)$_2$ solution remained unreacted in the cross-linked network.

It is anticipated that when the temperature reached 180 °C, (i) the glycerol reacted with Ni(NO$_3$)$_2$ and produced hydroxyl (OH$^-$) ions (eq 6), which furtherly converted to Ni(OH)$_2$; and (ii) the cross-linked network of Mn^{2+}, Mn^{3+} was converted into stable MnO$_2$ in the presence of dissolved oxygen.[38]

$$4C_3H_8O_3 + NO_3^- \rightarrow 4C_3H_6O_3 + NH_3 + OH^- + 2H_2O \tag{6}$$
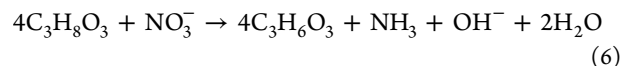
After forming those primary nanoparticles, their disordered self-aggregation started in between the GO surface. This is due to the hydrogen-bonding interaction between the primary nanoparticles of Ni(OH)$_2$ and MnO$_2$.[39] Subsequently, the GO reacted with glycerol and converted it into rGO during this hydrothermal process at 180 °C.[40] The self-aggregation of MnO$_2$ and Ni(OH)$_2$ on the converted rGO layers resulted in hybrid nanosheets of NMr. After 24 h of hydrothermal growth, those hybrid nanosheets are then expected to form a wrinkled nanostructure throughout the synthesized NMr composite. So, it is highly likely that the intercalation of Ni(OH)$_2$, MnO$_2$ contributed to expanding the rGO layers and assembling themselves into a turbostratic layered structure of NMr hybrid.

Morphology and Composition of the NMr. Surface morphologies of the as prepared ternary hybrid were studied using FESEM, and the micrographs are displayed in Figure 2a. It is observed that the ternary hybrid that the rGO layers were wrinkled flower-like and crumpled delaminating sheets. A high-temperature and pressure-driven hydrothermal process along with the strong van der Waals forces might be the reasons behind the way they are folded.[41] Furthermore, the presence of extremely disordered and randomly distributed hexagonal petal like nanoflakes were seen all over the hybrid structure as shown in the inset of the Figure 2a. The flakes are in the range of 80 to 90 nm in diameter with visible edges, and they tend to be layered or overlapped to construct the wrinkled flower-like shape. These randomly orientated nanosized flakes usually provide additional channels and exposing more active sites for electrolytic ions.[42] The growth formation of Ni(OH)$_2$ and
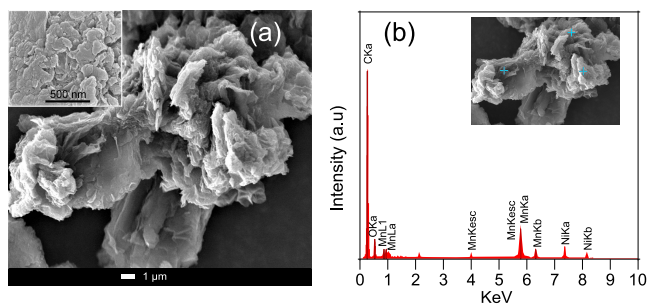
Figure 2. (a) SEM image of NMr composite, (b) EDX pattern showing with inset elemental mapping of NMr.

MnO_2 nanoparticles expanded the rGO layers which resulted in a thick chunk of NMr nanostructure. It is expected that the intercalation of controlled $Ni(OH)_2$ and MnO_2 nanoparticles prevented the agglomeration of rGO nanosheets and enhances the overall stability of the ternary hybrid. Now, the presence of $Ni(OH)_2$ and MnO_2 in between the rGO layers was also confirmed by EDX mapping (Figure 2b), indicating that the quantity of manganese and nickel contained in the rGO layers. The chemical composition of the NMr hybrid is presented in the Table S1.

The XRD results are shown in Figure 3a to confirm the phase of $Ni(OH)_2$ and MnO_2 in NMr hybrid. The well-defined peaks appeared at 23°, 36°, and 38°, indexed for γ-MnO_2 (JCPDS 14-0644),[43] whereas the peaks appeared at 26°, 33°, and 59° are indexed for α-$Ni(OH)_2$ (JCPDS 38-0715).[44] The AB stacking layers appeared in the XRD pattern of NMr at 10.2°, suggesting that the interlayer distance between two stacked rGO layers is 0.87 nm. The wider peak regions at 26.3°

also suggested the highly amorphous 002 planes of the as-prepared NMr hybrid. Here, a shifting in XRD peak for NMr hybrid is observed compared with the rGO. The main reason for shifting the NMr diffraction peaks from 22° to 26.3° compared with rGO is the increase/decrease in the lattice parameters that is reflected by the shift of diffraction peaks.[45] Additionally, the coexistence of 100 peaks at 43° indicates the turbostratic nature of the ternary hybrid. Comparing the XRD curves of pure rGO and NMr, it can be concluded that $Ni(OH)_2$ and MnO_2 nanoparticles were successfully intercalated in between the rGO layers, and the hybrid rGO sheets are wrinkled.

The Raman spectrum of the nanohybrid displayed in Figure 3b shows both the bands D and G bands of the rGO layer at 1337 and 1585 cm^{-1}, respectively. Another band that appeared at 542 to 675 cm^{-1} represents the Mn−O and Ni−O stretching vibration from MnO_2 and $Ni(OH)_2$. The G-band is triggered by the in-plane vibrations of sp2-bonded carbon atoms, whereas the D-band is caused by defects and disorder in carbon structures. The number of defects and degree of graphitization in the samples can be measured using the (I_D/I_G) ratio. The (I_D/I_G) ratio was 1.25, attributed to extensive curvature and wrinkled rGO layers. Usually, ordered rGO processes an (I_D/I_G) ratio below 1.0, and above this value, the disordered or defective flakes of graphite dominate over graphitic flakes.[46] In comparison with the Raman spectrum of rGO as shown in Figure 3b, it is clearly distinguished that the intercalation of $Ni(OH)_2$ and MnO_2 contributed in the enhancement of the I_D/I_G ratio in the ternary hybrid. The Raman spectrum suggests that the disordered carbon morphology is indeed turbostratic because of the peaks found in T1 and T2 regions.[47,48] This feature is exclusively
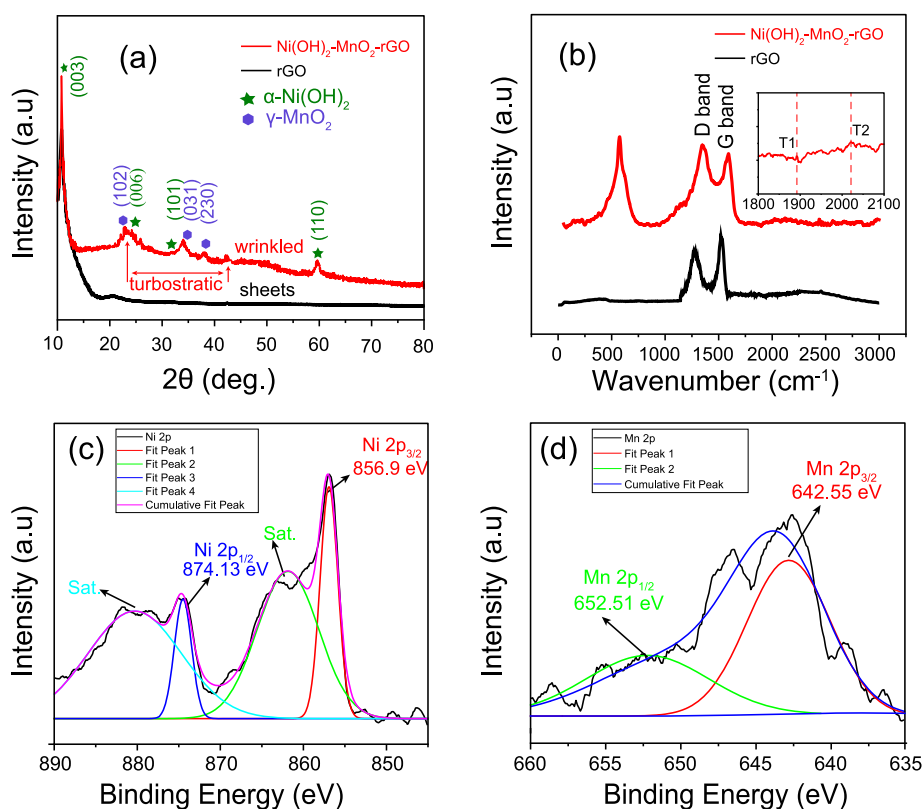

Figure 3. (a) XRD of NMr composite, (b) Raman spectrum of NMr composite, (c, d) Ni 2p and Mn 2p XPS spectra of NMr structure.
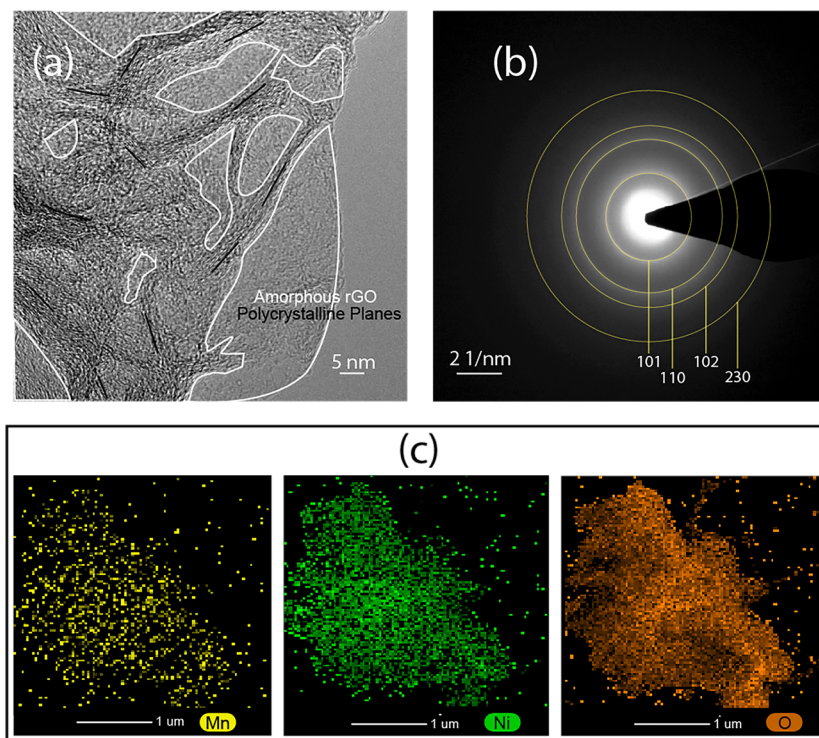
Figure 4. (a) HRTEM of hybrid nanosheets of NMr, (b) SAED pattern of the NMr sheet. (c) Chemical mapping of Mn, Ni, and O in the NMr.

attributed to the rotational mismatch of the neighboring rGO layers of the NMr hybrid and presumably due to the high-temperature hydrothermal process.

The survey spectrum of XPS in Figure S1a shows the elements (Mn, Ni, C, O) present in the as-prepared ternary hybrid. The percentage of these elements from XPS survey spectrum was also calculated and presented in Table S3. The XPS results in Figure 3c,d again support the information on the EDX and confirm the presence of the Mn, and Ni in the NMr. In Figure 3c, the two signals at 874.13 and 856.9 eV represent the Ni $2p_{1/2}$ and Ni $2p_{3/2}$ of $Ni(OH)_2$. The spectrum also shows two satellite (sat.) peaks with those spin−orbit peaks of Ni $2p_{1/2}$ and Ni $2p_{3/2}$. Figure 3d shows the Mn 2p XPS spectrum and shows the presence of $Mn_{3/2}$ at 642.55 eV and $Mn_{1/2}$ at 652.51 eV, respectively. Thus, those XPS results expose the coexistence of MnO_2 and $Ni(OH)_2$ in the as-prepared ternary hybrid of NMr. However, the disappearance of the peaks for carbonyl and ester in the C 1s spectrum shown in Figure S1b suggests that the GO was converted into rGO during the hydrothermal preparation.[49]

The HRTEM image in Figure 4a reveals rough and transparent nanosheets, which indicates the ultrathin nature of the hybrid nanostructure. The coexistence of crystalline and amorphous regions marked in Figure 4a defines the impregnation of crystalline $Ni(OH)_2$ and MnO_2 in the amorphous rGO sheets and thus confirms the heterostructure assembly. Besides, another TEM image with EDX analysis is presented in the Figure S2, which shows the ultrathin rGO layers consisting of manganese and nickel. The phase of those crystallites present in the hybrid can again be observed by the selected area electron diffraction (SAED) pattern shown in Figure 4b. Generally, amorphous material shows this kind of SAED pattern, and several dots appear for single-crystalline regions present in composites. Since single crystalline material has only a single orientation at equal spacing, an equal spaced

dots pattern can be observed. However, for polycrystalline materials, the grains have varying orientations so the equal spaced dot patterns can not be observed for the hybrid.[50,51] However, the SAED revealed the (101), (110) planes for $Ni(OH)_2$ and (102), (230) planes for MnO_2, respectively, and that again supports the XRD data shown in Figure 3a. The HRTEM image eventually supports the statements from the XRD, EDX, and FESEM images and proves the formation of $Ni(OH)_2$ and MnO_2 nanocrystals in between the rGO layers. However, in Figure 4c, the chemical mapping of the composite confirms that those layers contain rGO with Mn, Ni, and O contents in the total composite structures. The above characterizations thus prove that the as-prepared ternary hybrid of NMr has successfully been synthesized by adopting a simple hydrothermal approach. Additionally, it can be concluded that the improved heterostructured wrinkled flower-like and turbostratic nanostructure of NMr should be able to store an efficient amount of electrochemical energy.

Electrochemical Characterizations. As previously stated, the ternary NMr heterostructure has very specific morpho-logical and structural features, as well as outstanding properties, making them very promising candidates for advanced electrochemical capacitors. The electrochemical performance evaluation of NMr was conducted using CV, GCD, and EIS in an aqueous 0.5 M Na_2SO_4 electrolyte in a symmetric two-electrode setup. The resulting CV and GCD curves are shown in Figure 5. CV was conducted with different operating potential ranges of 0−1.2 V at a fixed scan rate of 20 mV s^{-1} to understand the electrochemical stable potential window (ESPW). It is observed that the CV shapes deviate from the perfect rectangular shape beyond the potential of 1.0 V because of the dissociation of water and O_2/H_2 gas evaluation, shown in Figure 5a.[34] Furthermore, the ESPW was confirmed from the GCD results of a fixed current density of 1.0 A g^{-1} as the shape of the GCD curve appeared symmetrical
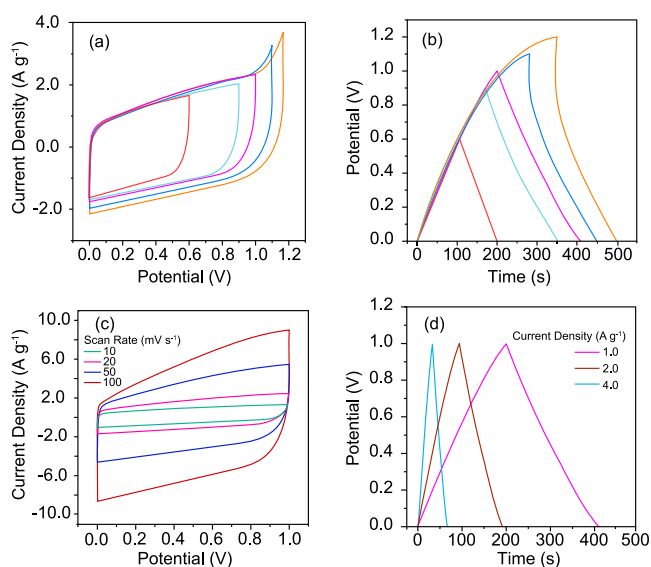
Figure 5. (a) CV at a fixed scan rate of 20 mV s^{-1} in the different potential windows, (b) GCD at 1 A g^{-1} by varying the potential window, (c) shows CV of NMr at different scan rates, and (d) GCD of NMr at different current densities.

triangle with extended discharge time within the potential of 1.0 V, shown in Figure 5b. The electrochemical rate capability of as prepared ternary hybrid was done by conducting CVs with different scan rates from 10 to 100 mV s^{-1}, and GCD performance was conducted at 1.0, 2.0, and 4.0 A g^{-1} within potential range 0 to 1 V, shown respectively in Figure 5c,d. At high scan rates, the hybrid electrode retained its CV shape, indicating the excellent reversibility, high-rate capability, and low internal resistance of the SC device.[36,52]

For a comparative analysis, we have presented the comparative CV and GCD profiles of NMr and rGO as shown in Figure 6a,b, respectively; CV at the scan rate of 20
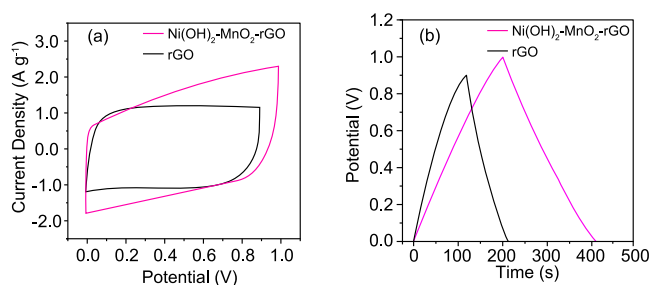

Figure 6. (a) Comparison of CV and (b) GCD of NMr composite and rGO.

mV s^{-1} and GCD at the current density of 1 A g^{-1}. The larger integrated CV area and longer discharge time of ternary NMr electrode, clearly confirm its superior charge storage ability and higher capacitance in comparison with rGO, which also comply with the outcomes of hybrid material. To validate these results further, we have performed the CV and GCD analyses of rGO electrodes shown in Figure S3a,b, respectively. However, significant redox peaks should have appeared because of the presence of Ni(OH)$_2$ and MnO$_2$ nanoparticles during the electrochemical process. However, there is significant evidence that showed the prominent redox peaks are mostly observed when an acidic or basic electrolyte is used

to measure the CV of electrode materials, especially in a hybrid like NMr. Usually, a neutral electrolyte in a two-electrode setup is not suitable for observing the redox peaks of Ni(OH)$_2$ persisting in a hybrid because of several reasons. For instance, in comparison with Na$_2$SO$_4$ and NaOH electrolytes, the redox peak is always dominant in NaOH because of the increased anionic size of sulfate ions (1.49 Å) as compared with hydroxyl ions (1.10 Å).[53] Another reason for the absence of redox peaks indicates that the supercapacitors are charged and discharged at a pseudoconstant rate over the entire voltammetric cycles, with the total capacitance arising from the redox pseudocapacitance of the loaded NMr coupled with the double-layer capacitances of the Ni(OH)$_2$, MnO$_2$, and rGO.[54,55]

The C_{sp} values of NMr and pristine rGO with different current densities are demonstrated in Figure 7a. A maximum
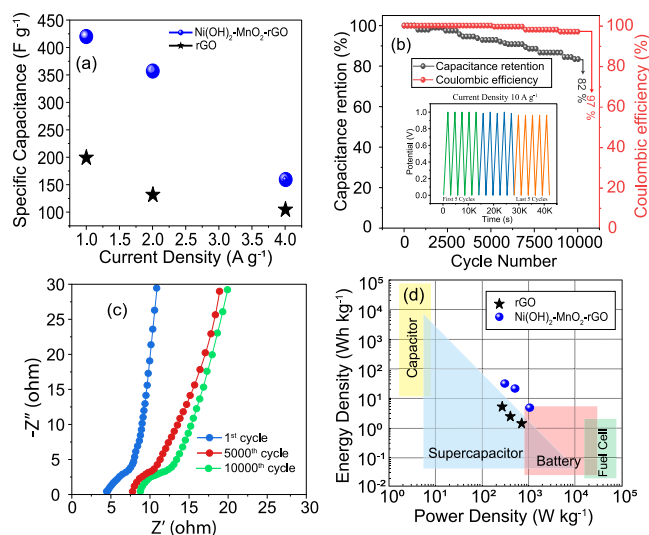

Figure 7. (a) C_{sp} vs current density, (b) cyclic stability test, (c) EIS analysis after different cycles, and (d) Ragone plot of NMr hybrid electrode.

C_{sp} of 420 F g^{-1} was achieved for ternary NMr heterostructured hybrid material at the current density of 1 A g^{-1}, almost 2.5-fold higher than the rGO (200 F g^{-1}) at the same current density. The synergistic effect of the MnO$_2$ and Ni(OH)$_2$ decoration in between the rGO layers is mainly responsible for the improved C_{sp} of the ternary hybrid. During the electrochemical process, the presence of pseudocapacitive nanoparticles induces extra energy storing capability by performing the redox reactions shown in eqs 7 and 8.[35,56] Those reactions offer adsorption and desorption of protons and electrolyte cations (Na$^+$ of Na$_2$SO$_4$) on the Ni(OH)$_2$ and MnO$_2$, respectively. Hence, it can be demonstrated that the growth of Ni(OH)$_2$ and MnO$_2$ in between the rGO surface facilitates better charge storing capability than pristine rGO.[57]

$$MnO_2 + Na^+ + e^- \leftrightarrow MnOONa \tag{7}$$

$$Ni(OH)_2 + OH^- \leftrightarrow NiOOH + H_2O + e^- \tag{8}$$

The electrochemical characteristics of the hybrid SC were also studied using EIS analysis. Figure S3c,d respectively displays the Nyquist plots and corresponding fitting circuit of the synthesized NMr and rGO, which were obtained by conducting EIS over a frequency band of 100 kHz to 0.01 Hz with an amplitude of 10 mV. The calculated charge transfer

Table 1. Comparison of the Electrochemical Performance of Nickel, Manganese, and rGO Based Binary/Ternary Electrode Materials and This Work

electrode materials	C_{sp} (F g^{-1}) (current density)	E (Wh kg^{-1})	P (W kg^{-1})	C_{sp} retention (cycles)	electrolyte	ref
WF-rGO	272 (0.5 A g^{-1})	8.2	500	91.5% (10000)	aqueous	60
Mn/Ni mixed oxides	210 (0.12 A g^{-1})	3.12	1000	96% (1000)	1.0 M Na$_2$SO$_4$	61
graphene-flower-like MnO$_2$	220 (0.5 A g^{-1})	84.4	396.3	98.3% (1000)	0.5 M Na$_2$SO$_4$ three-electrode system	62
graphene-MnO$_2$ nanostructured textiles	315 (2 mV s^{-1})	12.5	11000	95% (5000)	0.5 M Na$_2$SO$_4$	63
graphene porous NiO nanocomposite	430 (0.2 A g^{-1})	10.2	400	86.1% (2000)	6 M KOH	64
NMr	420 (1.0 A g^{-1})	14.68	250	82% (10000)	0.5 M Na$_2$SO$_4$	this work

kinetic parameters are tabulated in Table S2. Notably, the small R_s (4.70 Ω) and R_{ct} (12.20 Ω) values of the ternary hybrid confirmed a lower solution and charge transfer resistance compared to the pristine rGO; R_s (6.27 Ω) and R_{ct} (22.60 Ω) values were also evidence of its outstanding electrolyte accesibility. The expanded rGO layers in the ternary hybrid and enhanced conductivity owing to the nano-decoration of Ni(OH)$_2$ and MnO$_2$ contribute to the lesser resistance.

The long-term cyclic performance of the fabricated symmetric SC of the hybrid was investigated by repeating the GCD test 10 000 times at the current density of 10 A g^{-1} over the potential of 1.0 V, as demonstrated in Figure 7b. As can be observed, the hybrid SC exhibited 97% Coulombic efficiency and 82% capacitance retention of its specific capacitance after 10 000 cycles. Such a negligible loss in capacitance suggests a lesser deterioration in the chemical structure of ternary NMr hybrid and/or dissolution of MnO$_2$ during the cycling process.[58] The evidence of such facts is the increased electrochemical series resistance of 4.7 Ω to 8.4 Ω after the 10 000 cycles, as shown in Figure 7c. However, the Coulombic efficiency and the capacitance retention of ternary NMr electrode indicates its excellent long-term cyclic stability.

It is worth mentioning that the E and P of energy storage devices significantly impact their efficiency. We explored the correlation between the E and P of the assembled symmetric SC of ternary NMr materials. The findings have been illustrated using the Ragone plot in Figure 7d and compared to various energy-storage systems. The symmetric SC with the hybrid electrode delivered a maximum E of 14.58 Wh kg^{-1} and P of 250 W kg^{-1}. The nanodecoration of Ni(OH)$_2$ and MnO$_2$ between the rGO layers provides an expanded interlayer distance within the dense wrinkled hybrid rGO layers than the pristine rGO. More crucially, the presence of MnO$_2$ in this ternary hybrid resulted in the generation of numerous oxidation states, which brought about rich faradic reactions for pseudocapacitance. Additionally, the insertion of Ni(OH)$_2$ resulted in additional polarons, which resulted in a considerable increase in electrical conductivity. These poly-crystalline nanoparticles (Ni(OH)$_2$ and MnO$_2$) enable the hybrid material to achieve more energy density by facilitating different surfaces with nanodimensional tunnel structures.[59] The total summary of the electrochemical performance of pristine rGO and ternary NMr heterostructured hybrid is supplied in Table S3.

To the best knowledge, this is the highest specific capacitance reported for NMr hybrid electrode without using nickel foam current collector and any conductive additive. A comparison of the electrochemical performance of a few prior works is presented in Table 1 to compare this study. However, most existing works with higher specific capacitance are reported with either basic or acidic (KOH, H$_2$SO$_4$, or HCl) electrolytes. Those electrolytes are neither eco-friendly nor safer for fabricating long-lasting SC devices. Instead, this wrinkled flower-like NMr hybrid offers optimum energy density with a high power density and high cyclic stability using a cost-effective and safer aqueous Na$_2$SO$_4$ electrolyte system.

■ CONCLUSION

In summary, the study presented a facile and scalable synthesis route to prepare a ternary rGO hybrid intercalated with Ni(OH)$_2$ and MnO$_2$ nanoparticles in between rGO surfaces. The as-prepared NMr nanostructure having a distinguished structure, showed excellent electrochemical performance mainly because of its structural attributes. Furthermore, the *in situ* intercalation of Ni(OH)$_2$ and MnO$_2$ successfully prevented the interlayer stacking of rGO layers, and hence, the ternary hybrid exhibited a higher specific capacitance (420 F g^{-1}) than pure rGO sheets (200 F g^{-1}) at 1 A g^{-1} current density. More importantly, the ternary hybrid exhibited an energy density of 14.58 Wh kg^{-1} while maintaining a high-power density. Additionally, the electrode material showed excellent cyclic performance (10 000 cycles) at a higher current density like 10 A g^{-1}. This work provides a robust research aspect on TMO/H-rGO based ternary hybrid synthesis and morphological analysis for the fabrication of high-performance SC devices.

■ ASSOCIATED CONTENT

ⓢ Supporting Information

The Supporting Information is available free of charge at https://pubs.acs.org/doi/10.1021/acsomega.2c01986.

Survey XPS spectrum of NMr, C 1s XPS spectrum of NMr, TEM with EDX analysis, CV and GCD curves of pure rGO at different scan rates and current densities, comparsion of EIS for rGO and NMr, fitting circuit for both rGO and NMr, chemical composition for NMr hybrid, summarized EIS data of rGO and NMr, and total summary of electrochemical performance for rGO and NMr (PDF)

■ AUTHOR INFORMATION

Corresponding Author

Shakhawat H. Firoz − *Department of Chemistry, Bangladesh University of Engineering and Technology, Dhaka 1000,*

Bangladesh; orcid.org/0000-0002-1771-462X;
Email: shfiroz@chem.buet.ac.bd

Authors

Yeasin Arafat Tarek − *Department of Chemistry, Bangladesh University of Engineering and Technology, Dhaka 1000, Bangladesh;* orcid.org/0000-0003-2113-2486

Ragib Shakil − *Department of Chemistry, Bangladesh University of Engineering and Technology, Dhaka 1000, Bangladesh;* orcid.org/0000-0003-2212-7953

Akter Hossain Reaz − *Department of Chemistry, Bangladesh University of Engineering and Technology, Dhaka 1000, Bangladesh;* orcid.org/0000-0001-9508-710X

Chanchal Kumar Roy − *Department of Chemistry, Bangladesh University of Engineering and Technology, Dhaka 1000, Bangladesh;* orcid.org/0000-0001-9894-3477

Hasi Rani Barai − *School of Mechanical and IT Engineering, Yeungnam University, Gyeongsan 38541, Republic of Korea;* orcid.org/0000-0001-5915-8425

Complete contact information is available at:
https://pubs.acs.org/10.1021/acsomega.2c01986

Notes

The authors declare no competing financial interest.

■ REFERENCES

(1) Shao, Y.; El-Kady, M. F.; Sun, J.; Li, Y.; Zhang, Q.; Zhu, M.; Wang, H.; Dunn, B.; Kaner, R. B. Design and mechanisms of asymmetric supercapacitors. *Chem. Rev.* **2018**, *118*, 9233−9280.

(2) Winter, M.; Brodd, R. J. What are batteries, fuel cells, and supercapacitors? *Chem. Rev.* **2004**, *104*, 4245−4270.

(3) Song, J.; Chen, Y.; Cao, K.; Lu, Y.; Xin, J. H.; Tao, X. Fully controllable design and fabrication of three-dimensional lattice supercapacitors. *ACS Appl. Mater. Interfaces* **2018**, *10*, 39839−39850.

(4) Xu, Y.; Ruan, J.; Pang, Y.; Sun, H.; Liang, C.; Li, H.; Yang, J.; Zheng, S. Homologous strategy to construct high-performance coupling electrodes for advanced potassium-ion hybrid capacitors. *Nano-micro letters* **2021**, *13*, 14.

(5) Wang, F.; Wang, X.; Chang, Z.; Zhu, Y.; Fu, L.; Liu, X.; Wu, Y. Electrode materials with tailored facets for electrochemical energy storage. *Nanoscale Horizons* **2016**, *1*, 272−289.

(6) Kim, M.; Choi, J.; Oh, I.; Kim, J. Design and synthesis of ternary Co 3 O 4/carbon coated TiO 2 hybrid nanocomposites for asymmetric supercapacitors. *Phys. Chem. Chem. Phys.* **2016**, *18*, 19696−19704.

(7) Cheng, X.; Zhang, J.; Ren, J.; Liu, N.; Chen, P.; Zhang, Y.; Deng, J.; Wang, Y.; Peng, H. Design of a hierarchical ternary hybrid for a fiber-shaped asymmetric supercapacitor with high volumetric energy density. *J. Phys. Chem. C* **2016**, *120*, 9685−9691.

(8) Das, T.; Verma, B. Facile synthesis of bimetallic CuFe2O4 based ternary hybrid composites for supercapacitor electrodes and optimization of weight ratio of the individuals on the basis of their electrochemical performances. *Materials Technology* **2022**, 9685−9691.

(9) Wu, D.; Xie, X.; Zhang, Y.; Zhang, D.; Du, W.; Zhang, X.; Wang, B. MnO2/carbon composites for supercapacitor: synthesis and electrochemical performance. *Frontiers in Materials* **2020**, *7*, 2.

(10) Wei, W.; Cui, X.; Chen, W.; Ivey, D. G. Manganese oxide-based materials as electrochemical supercapacitor electrodes. *Chem. Soc. Rev.* **2011**, *40*, 1697−1721.

(11) Jiang, H.; Li, C.; Sun, T.; Ma, J. High-performance supercapacitor material based on Ni (OH) 2 nanowire-MnO 2 nanoflakes core-shell nanostructures. *Chem. Commun.* **2012**, *48*, 2606−2608.

(12) Xi, Y.; Wei, G.; Li, J.; Liu, X.; Pang, M.; Yang, Y.; Ji, Y.; Izotov, V. Y.; Guo, Q.; Han, W. Facile synthesis of MnO2-Ni (OH) 2 3D ridge-like porous electrode materials by seed-induce method for high-performance asymmetric supercapacitor. *Electrochim. Acta* **2017**, *233*, 26−35.

(13) Chen, H.; Hu, L.; Yan, Y.; Che, R.; Chen, M.; Wu, L. One-step fabrication of ultrathin porous nickel hydroxide-manganese dioxide hybrid nanosheets for supercapacitor electrodes with excellent capacitive performance. *Adv. Energy Mater.* **2013**, *3*, 1636−1646.

(14) Xie, Y. Electrochemical properties of sodium manganese oxide/ nickel foam supercapacitor electrode material. *Inorganic and Nano-Metal Chemistry* **2021**, 1−8.

(15) Chen, H.; Zeng, S.; Chen, M.; Zhang, Y.; Li, Q. A new insight into the rechargeable mechanism of manganese dioxide based symmetric supercapacitors. *RSC Adv.* **2017**, *7*, 8561−8566.

(16) Nguyen, T.; Boudard, M.; Rapenne, L.; Carmezim, M. J.; Montemor, M. F. Morphological changes and electrochemical response of mixed nickel manganese oxides as charge storage electrodes. *Journal of Materials Chemistry A* **2015**, *3*, 10875−10882.

(17) Wu, C.; Cai, J.; Zhu, Y.; Zhang, K. Hybrid reduced graphene oxide nanosheet supported Mn-Ni-Co ternary oxides for aqueous asymmetric supercapacitors. *ACS Appl. Mater. Interfaces* **2017**, *9*, 19114−19123.

(18) Karimi, A.; Kazeminezhad, I.; Naderi, L.; Shahrokhian, S. Construction of a ternary nanocomposite, polypyrrole/Fe-Co sulfide-reduced graphene oxide/nickel foam, as a novel binder-free electrode for high-performance asymmetric supercapacitors. *J. Phys. Chem. C* **2020**, *124*, 4393−4407.

(19) Chen, H.; Zhou, S.; Wu, L. Porous nickel hydroxide-manganese dioxide-reduced graphene oxide ternary hybrid spheres as excellent supercapacitor electrode materials. *ACS Appl. Mater. Interfaces* **2014**, *6*, 8621−8630.

(20) Purkait, T.; Singh, G.; Kumar, D.; Singh, M.; Dey, R. S. High-performance flexible supercapacitors based on electrochemically tailored three-dimensional reduced graphene oxide networks. *Sci. Rep.* **2018**, *8*, 640.

(21) Govindarajan, D.; Uma Shankar, V.; Gopalakrishnan, R. Supercapacitor behavior and characterization of RGO anchored V2O5 nanorods. *Journal of Materials Science: Materials in Electronics* **2019**, *30*, 16142−16155.

(22) Joshi, Y.; Umasankaran, A.; Klaassen, C.; AlAmer, M.; Joo, Y. L. Critical roles of reduced graphene oxide in the electrochemical performance of silicon/reduced graphene oxide hybrids for high rate capable lithium-ion battery anodes. *Electrochim. Acta* **2022**, *404*, 139753.

(23) Zhao, B.; Chen, D.; Xiong, X.; Song, B.; Hu, R.; Zhang, Q.; Rainwater, B. H.; Waller, G. H.; Zhen, D.; Ding, Y.; et al. A high-energy, long cycle-life hybrid supercapacitor based on graphene composite electrodes. *Energy Storage Materials* **2017**, *7*, 32−39.

(24) Wang, C.; Vinodgopal, K.; Dai, G.-P. Large-area synthesis and growth mechanism of graphene by chemical vapor deposition. *Chem. Vap. Depos. Nanotechnol* **2018**, *5*, 97−113.

(25) Lesiak, B.; Trykowski, G.; Tóth, J.; Biniak, S.; Kövér, L.; Rangam, N.; Stobinski, L.; Malolepszy, A. Chemical and structural properties of reduced graphene oxideependence on the reducing agent. *J. Mater. Sci.* **2021**, *56*, 3738−3754.

(26) Smith, A. T.; LaChance, A. M.; Zeng, S.; Liu, B.; Sun, L. Synthesis, properties, and applications of graphene oxide/reduced

graphene oxide and their nanocomposites. *Nano Materials Science* **2019**, *1*, 31−47.

(27) Sreeprasad, T. S.; Maliyekkal, S. M.; Lisha, K. P.; Pradeep, T. Reduced graphene oxide-metal/metal oxide composites: facile synthesis and application in water purification. *Journal of hazardous materials* **2011**, *186*, 921−931.

(28) Jin, S.; Chung, B.; Park, H. J.; Cunning, B. V.; Lee, J.-H.; Yoon, A.; Huang, M.; Seo, H.; Lee, D.; Lee, Z.; et al. Ultrahigh Strength and Modulus Graphene-Based Hybrid Carbons with AB-Stacked and Turbostratic Structures. *Adv. Funct. Mater.* **2020**, *30*, 2005381.

(29) Purkait, T.; Singh, G.; Singh, M.; Kumar, D.; Dey, R. S. Large area few-layer graphene with scalable preparation from waste biomass for high-performance supercapacitor. *Sci. Rep.* **2017**, *7*, 15239.

(30) Wang, Z.; Hu, Y.; Liu, W.; Xu, L.; Guan, M.; Zhao, Y.; Bao, J.; Li, H. Manganese-Modulated Cobalt-Based Layered Double Hydroxide Grown on Nickel Foam with 1D-2D-3D Heterostructure for Highly Efficient Oxygen Evolution Reaction and Urea Oxidation Reaction. *Chem.—Eur. J.* **2020**, *26*, 9382−9388.

(31) Liu, X.; Wang, J.; Yang, G. Amorphous nickel oxide and crystalline manganese oxide nanocomposite electrode for transparent and flexible supercapacitor. *Chemical Engineering Journal* **2018**, *347*, 101−110.

(32) Sharma, N.; Sharma, V.; Jain, Y.; Kumari, M.; Gupta, R.; Sharma, S.; Sachdev, K. Synthesis and characterization of graphene oxide (GO) and reduced graphene oxide (rGO) for gas sensing application. *Macromol. Symp.* **2017**, *376*, 1700006.

(33) Tarek, Y. A.; Reaz, A. H.; Shakil, R.; Roy, H.; Jahan, R. A.; Roy, C. K.; Firoz, S. H. One-Step Gel Formation Method for the Synthesis of NiO-Mn X O Y Mixed Oxide Nanomaterials as a Prospective Supercapacitor Material. *2020 2nd International Conference on Sustainable Technologies for Industry 4.0 (STI)*; Dhaka, Bangladesh, December 19-20, 2020; pp 1−6.

(34) Shakil, R.; Shaikh, M. N.; Shah, S. S.; Reaz, A. H.; Roy, C. K.; Chowdhury, A.-N.; Aziz, M. A. Development of a Novel Bio-based Redox Electrolyte using Pivalic Acid and Ascorbic Acid for the Activated Carbon-based Supercapacitor Fabrication. *Asian Journal of Organic Chemistry* **2021**, *10*, 2220−2230.

(35) Reaz, A. H.; Saha, S.; Roy, C. K.; Wahab, M. A.; Will, G.; Amin, M. A.; Yamauchi, Y.; Liu, S.; Kaneti, Y. V.; Hossain, M. S.; Firoz, S. H. Boosting capacitive performance of manganese oxide nanorods by decorating with three-dimensional crushed graphene. *Nano Convergence* **2022**, *9*, 1−12.

(36) Barai, H. R.; Reaz, A. H.; Tarek, Y. A.; Saha, S.; Mojumder, M. N.; Chowdhury, K.; Firoz, S. H.; Joo, S. W.; Roy, C. K. Communication-Self-Doped Mesoporous Activated Carbon Prepared from Car Exhaust Exhibited Long Cycle Life and High Specific Capacitance for Supercapacitor Applications. *ECS Journal of Solid State Science and Technology* **2021**, *10*, 071014.

(37) Ullah, A. A.; Kibria, A. F.; Akter, M.; Khan, M.; Maksud, M.; Jahan, R. A.; Firoz, S. H. Synthesis of Mn3O4 nanoparticles via a facile gel formation route and study of their phase and structural transformation with distinct surface morphology upon heat treatment. *Journal of Saudi Chemical Society* **2017**, *21*, 830−836.

(38) Shimamura, N.; Kanda, R.; Matsukubo, Y.; Hirai, Y.; Abe, H.; Hirai, Y.; Yoshida, T.; Yabu, H.; Masuhara, A. Preparation of Hierarchic Porous Films of α-MnO2 Nanoparticles by Using the Breath Figure Technique and Application for Hybrid Capacitor Electrodes. *ACS omega* **2019**, *4*, 3827−3831.

(39) Yang, L.-X.; Zhu, Y.-J.; Tong, H.; Liang, Z.-H.; Wang, W.-W. Hierarchical β-Ni (OH) 2 and NiO carnations assembled from nanosheet building blocks. *Cryst. Growth Des.* **2007**, *7*, 2716−2719.

(40) Dreyer, D. R.; Murali, S.; Zhu, Y.; Ruoff, R. S.; Bielawski, C. W. Reduction of graphite oxide using alcohols. *J. Mater. Chem.* **2011**, *21*, 3443−3447.

(41) Alli, U.; Hettiarachchi, S. J.; Kellici, S. Chemical functionalisation of 2D materials by batch and continuous hydrothermal flow synthesis. *Chem.—Eur. J.* **2020**, *26*, 6447−6460.

(42) Ambrosi, A.; Chua, C. K.; Bonanni, A.; Pumera, M. Electrochemistry of graphene and related materials. *Chem. Rev.* **2014**, *114*, 7150−7188.

(43) Huang, J.; Dai, Y.; Singewald, K.; Liu, C.-C.; Saxena, S.; Zhang, H. Effects of MnO2 of different structures on activation of peroxymonosulfate for bisphenol A degradation under acidic conditions. *Chemical Engineering Journal* **2019**, *370*, 906−915.

(44) Yang, H.; Gong, L.; Wang, H.; Dong, C.; Wang, J.; Qi, K.; Liu, H.; Guo, X.; Xia, B. Y. Preparation of nickel-iron hydroxides by microorganism corrosion for efficient oxygen evolution. *Nat. Commun.* **2020**, *11*, 5075.

(45) Xu, J.; Li, D.; Chen, Y.; Tan, L.; Kou, B.; Wan, F.; Jiang, W.; Li, F. Constructing sheet-on-sheet structured graphitic carbon nitride/ reduced graphene oxide/layered MnO2 ternary nanocomposite with outstanding catalytic properties on thermal decomposition of ammonium perchlorate. *Nanomaterials* **2017**, *7*, 450.

(46) Chang, S.-J.; Hyun, M. S.; Myung, S.; Kang, M.-A.; Yoo, J. H.; Lee, K. G.; Choi, B. G.; Cho, Y.; Lee, G.; Park, T. J. Graphene growth from reduced graphene oxide by chemical vapour deposition: seeded growth accompanied by restoration. *Sci. Rep.* **2016**, *6*, 22653.

(47) Luong, D. X.; Bets, K. V.; Algozeeb, W. A.; Stanford, M. G.; Kittrell, C.; Chen, W.; Salvatierra, R. V.; Ren, M.; McHugh, E. A.; Advincula, P. A.; et al. Gram-scale bottom-up flash graphene synthesis. *Nature* **2020**, *577*, 647−651.

(48) Garlow, J. A.; Barrett, L. K.; Wu, L.; Kisslinger, K.; Zhu, Y.; Pulecio, J. F. Large-area growth of turbostratic graphene on Ni (111) via physical vapor deposition. *Sci. Rep.* **2016**, *6*, 19804.

(49) Johra, F. T.; Jung, W.-G. Hydrothermally reduced graphene oxide as a supercapacitor. *Appl. Surf. Sci.* **2015**, *357*, 1911−1914.

(50) Tang, Q.; Ma, L.; Cao, F.; Gan, M.; Yan, F. Different morphologies of Ni (OH) 2 derived from a MOF template for high performance supercapacitors. *Journal of Materials Science: Materials in Electronics* **2019**, *30*, 9114−9122.

(51) Nguyen, T.; Boudard, M.; Carmezim, M. J.; Montemor, M. F. Layered Ni (OH) 2-Co (OH) 2 films prepared by electrodeposition as charge storage electrodes for hybrid supercapacitors. *Sci. Rep.* **2017**, *7*, 39980.

(52) Reaz, A. H.; Barai, H. R.; Saha, S.; Chowdhury, K.; Mojumder, M. N.; Firoz, S. H.; Chowdhury, A.-N.; Joo, S. W.; Roy, C. K. Self-Doped Activated Carbons from Car Exhaust as High-Performance Supercapacitor Electrode Materials for Sustainable Energy Storage System. *J. Electrochem. Soc.* **2021**, *168*, 080535.

(53) Nithya, V.D.; Kalai Selvan, R.; Kalpana, D.; Vasylechko, L.; Sanjeeviraja, C. Synthesis of Bi2WO6 nanoparticles and its electrochemical properties in different electrolytes for pseudocapacitor electrodes. *Electrochim. Acta* **2013**, *109*, 720−731.

(54) Liao, Q.; Li, N.; Jin, S.; Yang, G.; Wang, C. All-solid-state symmetric supercapacitor based on Co3O4 nanoparticles on vertically aligned graphene. *ACS Nano* **2015**, *9*, 5310−5317.

(55) Lang, X.; Hirata, A.; Fujita, T.; Chen, M. Nanoporous metal/ oxide hybrid electrodes for electrochemical supercapacitors. *Nature Nanotechnol.* **2011**, *6*, 232−236.

(56) Roy, C. K.; Shah, S. S.; Reaz, A. H.; Sultana, S.; Chowdhury, A.-N.; Firoz, S. H.; Zahir, M. H.; Ahmed Qasem, M. A.; Aziz, M. A. Preparation of Hierarchical Porous Activated Carbon from Banana Leaves for High-performance Supercapacitor: Effect of Type of Electrolytes on Performance. *Chemistry-An Asian Journal* **2021**, *16*, 296−308.

(57) Min, S.; Zhao, C.; Zhang, Z.; Wang, K.; Chen, G.; Qian, X.; Guo, Z. Hydrothermal growth of MnO 2/RGO/Ni (OH) 2 on nickel foam with superior supercapacitor performance. *RSC Adv.* **2015**, *5*, 62571−62576.

(58) Pender, J. P.; Jha, G.; Youn, D. H.; Ziegler, J. M.; Andoni, I.; Choi, E. J.; Heller, A.; Dunn, B. S.; Weiss, P. S.; Penner, R. M.; et al. Electrode degradation in lithium-ion batteries. *ACS Nano* **2020**, *14*, 1243−1295.

(59) Lin, T.-W.; Dai, C.-S.; Hung, K.-C. High energy density asymmetric supercapacitor based on NiOOH/Ni3S2/3D graphene and Fe3O4/graphene composite electrodes. *Sci. Rep.* **2014**, *4*, 7274.

(60) Lai, L.; Su, S.; Li, R.; Dai, H.; Zhu, X. Wrinkled Flower-Like Reduced Graphene Oxide for High-Performance Supercapacitors. *ChemistrySelect* **2020**, *5*, 7113−7120.

(61) Kim, H.; Popov, B. N. Synthesis and characterization of MnO2-based mixed oxides as supercapacitors. *J. Electrochem. Soc.* **2003**, *150*, D56.

(62) Dong, J.; Lu, G.; Wu, F.; Xu, C.; Kang, X.; Cheng, Z. Facile synthesis of a nitrogen-doped graphene flower-like MnO2 nano-composite and its application in supercapacitors. *Appl. Surf. Sci.* **2018**, *427*, 986−993.

(63) Yu, G.; Hu, L.; Vosgueritchian, M.; Wang, H.; Xie, X.; McDonough, J. R.; Cui, X.; Cui, Y.; Bao, Z. Solution-processed graphene/MnO2 nanostructured textiles for high-performance electrochemical capacitors. *Nano Lett.* **2011**, *11*, 2905−2911.

(64) Jiang, Y.; Chen, D.; Song, J.; Jiao, Z.; Ma, Q.; Zhang, H.; Cheng, L.; Zhao, B.; Chu, Y. A facile hydrothermal synthesis of graphene porous NiO nanocomposite and its application in electrochemical capacitors. *Electrochim. Acta* **2013**, *91*, 173−178.